

## Optimization of crystallographic texture for sheet-forming applications using Taylor-based Models

Galán-López, Jesús; Kestens, Leo A.I.

**DOI**

[10.1007/s11661-018-4869-8](https://doi.org/10.1007/s11661-018-4869-8)

**Publication date**

2018

**Document Version**

Final published version

**Published in**

Metallurgical and Materials Transactions A: Physical Metallurgy and Materials Science

**Citation (APA)**

Galán-López, J., & Kestens, L. A. I. (2018). Optimization of crystallographic texture for sheet-forming applications using Taylor-based Models. *Metallurgical and Materials Transactions A: Physical Metallurgy and Materials Science*, 49(11), 5745-5762. <https://doi.org/10.1007/s11661-018-4869-8>

**Important note**

To cite this publication, please use the final published version (if applicable).  
Please check the document version above.

**Copyright**

Other than for strictly personal use, it is not permitted to download, forward or distribute the text or part of it, without the consent of the author(s) and/or copyright holder(s), unless the work is under an open content license such as Creative Commons.

**Takedown policy**

Please contact us and provide details if you believe this document breaches copyrights.  
We will remove access to the work immediately and investigate your claim.

# Optimization of Crystallographic Texture for Sheet-forming Applications Using Taylor-based Models



JESÚS GALÁN-LÓPEZ and LEO A.I. KESTENS

Plastic deformation of metallic materials is an inherently anisotropic process as a result of the presence of preferential orientations in their crystallographic texture. Crystal plasticity modeling, which allows simulating the response of polycrystal aggregates taking into account their texture and other microstructural parameters, has been extensively used to predict this behavior. In this work, crystal plasticity models are used to deal with the opposite problem: given a desired behavior, determine how to modify a texture to approximate this behavior in the most efficient way. This goal can be expressed as an optimization problem, in which the objective is to find the texture with the best formability properties among all the possible ones. An incremental optimization method, based on the gradient descent algorithm, has been developed and applied to different initial textures corresponding to typical steel and aluminum sheet products. According to expectations, the textures found present a stronger  $\gamma$  fiber component. Moreover, the method sets the basis for the development of more complicated optimization schemes directed toward optimizing specific materials and forming processes.

<https://doi.org/10.1007/s11661-018-4869-8>  
© The Author(s) 2018

## I. INTRODUCTION

SHEET metal forming is one of the main manufacturing processes in industry worldwide. Deep drawing of metal sheets is an essential operation in the production of vehicles, many construction elements and electronic devices, and industrial and home appliances. It is therefore essential to know how the properties of a metal sheet affect its capacity to be deformed and the quality of the final products. Indeed, the scientific community has extensively studied all kinds of problems related with sheet metal forming,<sup>[1]</sup> making use of the most advanced techniques in the fields of finite element modeling<sup>[2]</sup> and crystallographic texture analysis<sup>[3]</sup> as they have become available.

To obtain the best results in a deep-drawing process, a metal sheet must deform with a specific anisotropic behavior. An ideal sheet would be one that can accommodate any arbitrary shape without experiencing any variation in thickness. More realistically, metal sheets used in industrial processes are selected such that the strain in the direction normal to the sheet plane takes a value as low and uniform as possible.

### A. Quantitative Indicators of Formability

Several magnitudes have been proposed to quantify the formability of metal sheets.<sup>[4]</sup> The Lankford coefficients, or  $r$  values,<sup>[5]</sup> and the contraction ratios, or  $q$  values, defined by Bunge,<sup>[6]</sup> are both widely used. Although these parameters are not an intrinsic material property, but affected by external factors such as specimen geometry and applied strain,<sup>[7,8]</sup> it is possible to use  $r$  and  $q$  values to compare different materials as long as these factors are carefully controlled. The  $r$  and  $q$  values are correlated, but  $r$  values present some inconvenience when used for quantitative data analysis<sup>[9]</sup>—in particular for optimization problems—because of the possibility of infinite values. For convenience, only  $q$  values will be used in the following.

Optimal formability properties will be obtained when the  $q$  value in every direction parallel to the sheet plane is equal to one. In practice, the aim is that the  $q$  values become as high as possible, while being the same for every direction. This condition will be evaluated using

---

JESÚS GALÁN-LÓPEZ is with the Materials Innovation Institute M2i, Van der Burghweg 1, 2628 CS, Delft, The Netherlands and also with the Materials Science and Engineering Department, Faculty 3mE, Delft University of Technology, Mekelweg 2, 2628 CD, Delft, The Netherlands. Contact e-mail: [j.galanlopez@m2i.nl](mailto:j.galanlopez@m2i.nl) LEO A.I. KESTENS is with the Materials Science and Engineering Department, Faculty 3mE, Delft University of Technology and also with the Department of Materials Science and Engineering, Faculty of Engineering and Architecture, Ghent University, Technologiepark 903, Zwijnaarde, 9052, Ghent, Belgium.

Manuscript submitted April 12, 2018.

the arithmetic mean and standard deviation of all the  $q$  values between 0 and 90 degrees at 15-degree intervals\*.

---

\*The more traditional  $\bar{q}$  and  $\Delta q$  indicators, calculated on the basis of the  $q_0$ ,  $q_{45}$  and  $q_{90}$  values only, are not used here to avoid incorrectly interpreting the cases for which  $q_0 + q_{90} = 2q_{45}$  as lack of planar anisotropy.

---

These magnitudes will be represented with the symbols  $\mu_q$  and  $\sigma_q$ , respectively, defined as:

$$\mu_q = \frac{1}{12} \left( q_0 + 2 \sum_{i=1}^5 q_{15i} + q_{90} \right) \quad [1a]$$

$$\sigma_q = \frac{1}{12} \sqrt{(q_0 - \mu_q)^2 + 2 \sum_{i=1}^5 (q_{15i} - \mu_q)^2 + (q_{90} - \mu_q)^2} \quad [1b]$$

Optimum formability will correspond to the case for which all the  $q$  values are one, which implies  $\mu_q = 1$  and  $\sigma_q = 0$ .

### B. Crystal Plasticity Modeling

Several crystal plasticity models have been developed<sup>[3,10]</sup> to perform predictions of how the mechanical properties and texture of polycrystalline materials evolve with plastic deformation. Although some of the models available nowadays are based on much more elaborated premises than the first models proposed by Taylor and Sachs,<sup>[11,12]</sup> the models based on these theories<sup>[13]</sup> still offer one of the best compromises between accuracy and complexity.

Initially, the models based on the Taylor theory were only applied to individual crystal orientations and sharp textures.<sup>[14–16]</sup> Further developments by Van Houtte allowed performing simulations involving arbitrary textures<sup>[17]</sup> and using these models to predict formability properties.<sup>[13,18,19]</sup> For example, Schouwenaars *et al.* showed that Taylor models can successfully predict the  $r$  values for different low-carbon steel sheets, the evolution of texture during tensile deformation, and also the evolution of the  $r$  values.<sup>[9]</sup> In more recent studies, Wronskia and Bacroix applied the Taylor–Bishop–Hill theory to study asymmetrically rolled steel to determine the formability obtained using different rolling parameters.<sup>[20]</sup> This theory has also been applied to the investigation of aluminum sheets,<sup>[21,22]</sup> and the results are comparable to those obtained by more complicated plasticity models. Another example is the work of An *et al.*, where different versions of the Taylor model were used for the calculation of yield loci used in FE simulations.<sup>[23]</sup>

Nevertheless, the Taylor theory also has some limitations. For example, Wu *et al.* showed that the method does not produce acceptable results when applied to prestrained aluminum.<sup>[24]</sup> More generally, Yoshinaga and coworkers proved that the Taylor theory produces

poor results when applied to model very sharp textures.<sup>[25]</sup> In this case, more advanced models are required in which grain morphology is taken into account, as shown by Delannay and Barnett.<sup>[26]</sup>

Other researchers have dealt with the problem using an analytical approach, completely phenomenologic such as Rees,<sup>[27]</sup> in combination with the Taylor model as done by Huang and Man<sup>[28]</sup> or applying advanced hardening laws as in the work of Lee *et al.*<sup>[29,30]</sup> Recently, more advanced crystal plasticity models have been developed, which take into account the neighborhood of each grain to calculate the behavior of the polycrystal. These models have been proved useful for the calculation of anisotropy of metal sheets, as for instance in the work of Sidor *et al.*<sup>[22]</sup> which shows that the most accurate predictions of  $r$  values for aluminum sheets subjected to asymmetric rolling are obtained using the ALAMEL model,<sup>[22]</sup> although only marginally better than using models based on the Taylor theory (or VPSC). Other models that have been tried in this context include the VPSC model,<sup>[22,31]</sup> a combination of Taylor with ALAMEL used by Gawad *et al.*<sup>[32,33]</sup> or the N-site interaction model by Delannay, Kalidindi and Van Houtte.<sup>[34]</sup> Even full-field solutions using crystal plasticity finite element modeling (CPFEM) have been applied to the problem by the group of Raabe and Roters in the Max-Planck Institut für Eisenforschung<sup>[35]</sup> and also using crystal plasticity fast Fourier transforms (CPFPT) to solve crystal plasticity problems in the frequency domain.<sup>[36]</sup> But it should be noted that a higher level of complexity does not always translate into a more accurate solution.

### C. Optimization of Crystallographic Texture

Although some researchers have identified theoretical maxima for  $r$  values at simplified conditions (for example, O'Brien *et al.* found in Reference 37 a maximum of  $r = 3$  for an ideal [111] texture), not many published studies specifically consider the problem of finding the ideal texture for optimum formability. Studies by Delannay *et al.* have attempted to optimize textures using a components-based description,<sup>[38]</sup> but the range of textures that can be represented by this method is limited. The most notable effort to date is the microstructure-sensitive design methodology by Adams *et al.*, which attempts to solve the problem defining the set of possible solutions in the Fourier space, first applied to the optimization of texture for improved elastic properties<sup>[39]</sup> and later extended to cover a full range of microstructural features and the optimization of different thermal and mechanical properties.<sup>[40]</sup> More recently, Liu and coworkers from MIT presented a machine-learning approach that was applied to the optimization of a Fe-Ga alloy microstructure for enhanced elastic, plastic and magnetostrictive properties.<sup>[41]</sup> The most important advantage of this method, which is its capacity to find global optima, is also its biggest drawback, since it is not immediately obvious how this information could be applied to improve an existing texture.

## D. Overview

In this article, a new optimization method for the improvement of the formability properties of textures is presented. After this introduction, the texture analysis and crystal plasticity methods used are described as well as how the gradient descent algorithm has been implemented for the optimization of a generic function dependent on texture and for the particular problem of sheet formability. The method is then applied to the optimization of several typical BCC and FCC textures. Finally, the obtained results are discussed and some final conclusions are derived.

## II. OPTIMIZATION METHOD AND MODELING

The goal of the optimization method is to find how to modify an existing texture to improve its formability. More specifically, the method will determine how this texture must be altered to improve its associated  $g$  values as predicted by a given crystal plasticity model, which in this case will be a model based on the Taylor–Bishop–Hill theory. However, to present the problem in the most general way, the method is first introduced for a general objective function and later specialized for the case of sheet formability.

### A. Orientation Distribution Function

The starting point of the optimization is an initial texture. This texture can be the result of a measurement in an existing material, performed using the electron-back-scatter-diffraction (EBSD) or X-ray diffraction (XRD) techniques, or a modeled texture, as, for example, a perfectly random texture or a fiber texture. In practice, a given texture will be represented by its associated orientation distribution function (ODF), which correlates an intensity (or probability) with each possible orientation. This function can be expressed as a series expansion using the harmonic method of Bunge<sup>[42]</sup>:

$$g(\varphi_1, \Phi, \varphi_2) = \sum_{l=0}^{\infty} \sum_{m=-l}^{+l} \sum_{n=-l}^{+l} C_l^{mn} T_l^{mn}(\varphi_1, \Phi, \varphi_2) \quad [2]$$

where an orientation is defined by the three Euler angles  $(\varphi_1, \Phi, \varphi_2)$ , the functions  $T_l^{mn}(\varphi_1, \Phi, \varphi_2)$  are the generalized spherical harmonics of order  $l, m, n$ , which are known, and the  $C_l^{mn}$  coefficients—called *C-coefficients*—are a set of coefficients that unequivocally define a texture.

Theoretically, expression [2] defines an infinite series. In practice, only a finite number of terms of the series expansion can be used. For cubic materials, it is known that  $l = 22$  usually is a sensible value, since it offers enough accuracy for most purposes and, as Bunge proved, is the maximum that can be determined by conventional XRD characterization techniques.<sup>[42]</sup> As a consequence of truncating the series, the estimated ODF is sharper than the real function. On the one hand, for certain orientations, the ODF will take negative values,

which is obviously incorrect in a probability function. On the other hand, the negative values have associated opposite values, which are overestimations of the real ODF, commonly called “ghost peaks.”

Different methods have been developed to correct an existing ODF to guarantee its positivity and eliminate the associated ghost peaks. The exponential method presented in Reference 43 consists of two phases: in the first one, the GHOST method,<sup>[44]</sup> is used to find an initial approximation. Then, non-negativity of the ODF is enforced by minimizing the error with respect to an exponential (always positive) function. This two-step procedure will be the one used in this work whenever a texture needs to be corrected. Nevertheless, it has to be noted that applying the ghost correction method inevitably smooths the function. Therefore, negative values and ghost peaks cannot be completely eliminated, and a compromise must be made.

In this work, the MTM-FHM software for texture analysis,<sup>[45]</sup> developed by Van Houtte in KU Leuven, has been used for the calculation of ODFs, its graphic representation and ghost correction\*\*. All the ODFs are

---

\*\*Some programs have been slightly modified, for example, to output their results with higher precision or produce ODF graphs with a consistent color scale.

---

calculated using  $l = 22$ , and negative values in the ODF are allowed only if (in absolute value) they are less than 10 pct of the maximum.

### B. Texture Optimization Using the Gradient Descent Method

The goal of the optimization process is to find the texture for which an objective function is minimized (maximization and other problems can be easily expressed as a minimization problem). In the most general form, this function will be a vector-valued function, such that each of its components is defined as a multivariate function of the C-coefficients. The problem consists in finding the set of coefficients that minimize all the components of the objective function. When optimizing a crystallographic texture, and specially if this texture corresponds to a commercial product, the possibilities to modify the processing method usually are very limited. Additional conditions can be introduced in the problem in the form of constraints, but it will still be desirable to know how a current texture can be modified to improve its properties in the most efficient manner, what the obtained improvement would be, and how the original texture can be gradually modified to reach this goal. Therefore, the gradient descent methods will be preferred instead of a derivative-free optimization. The necessary constraints will highly depend on the specific process and therefore will not be treated here.

It is acknowledged that a gradient descent method is only able to find local minima. However, the solution approaches these minima in the fastest possible manner, such that a maximum improvement is obtained with

small, incremental modifications. In practice, the capacity to modify existing production methods is very limited; therefore, it is of more interest to find how to improve an existing texture in the most efficient way than in the right direction to reach a theoretical global minimum that will most likely correspond to an extremely sharp texture, impossible to obtain with current techniques. In case it is possible to further improve from a local minimum, the method can be extended, for example, using simulated annealing techniques<sup>[46]</sup> or a stochastic gradient method.<sup>[47]</sup>

In a gradient descent method, the minimum is approximated first calculating (or estimating) the gradient of the function to optimize and then using this gradient to find a new solution that reduces the error in the direction of maximum descent. In the case of texture optimization, textures are represented by their ODF and, therefore, it can be considered that the objective function  $\mathbf{F}$ , of  $m$  components, takes as input a set of  $n$  C-coefficients ( $\mathbf{F} = \mathbf{F}(\mathbf{C})$ ). A first-order (linear) estimation of the gradient of the function,  $\nabla\mathbf{F}(\mathbf{C})$ , is then calculated as:

$$\begin{aligned} \nabla\mathbf{F}_{ij}(\mathbf{C}) &= \frac{\partial\mathbf{F}_i(\mathbf{C})}{\partial\mathbf{C}_j} \\ &= \begin{bmatrix} \partial\mathbf{F}_1(\mathbf{C})/\partial\mathbf{C}_j \\ \partial\mathbf{F}_2(\mathbf{C})/\partial\mathbf{C}_j \\ \vdots \\ \partial\mathbf{F}_m(\mathbf{C})/\partial\mathbf{C}_j \end{bmatrix} \approx \begin{bmatrix} (\mathbf{F}_1(\mathbf{C}'_j) - \mathbf{F}_1(\mathbf{C}))/\Delta c \\ (\mathbf{F}_2(\mathbf{C}'_j) - \mathbf{F}_2(\mathbf{C}))/\Delta c \\ \vdots \\ (\mathbf{F}_m(\mathbf{C}'_j) - \mathbf{F}_m(\mathbf{C}))/\Delta c \end{bmatrix} \end{aligned} \quad [3]$$

with  $\mathbf{C}'_j = \mathbf{C}_1, \mathbf{C}_2, \dots, \mathbf{C}_j + \Delta\mathbf{c}, \dots, \mathbf{C}_n$ , where  $\Delta c$  represents a small perturbation applied to the coefficient  $j$ . In theory, this linear approximation will approach the exact derivative when  $|\Delta c| \rightarrow 0$ , and therefore it is desirable that  $\Delta c$  is as low as possible. However, if the variation applied is too low, the deviation may be of the order of numerical fluctuations, leading to an erroneous gradient estimation. Again, it will be necessary to find a compromise solution.

Once the estimation of the gradient is available, the direction of maximum descent is obtained solving  $\Delta\mathbf{C}$  in the following linear system:

$$-\mathbf{F}(\mathbf{C}) = \nabla\mathbf{F}(\mathbf{C}) \Delta\mathbf{C} \quad [4]$$

Since, in most problems, the number of C-coefficients  $n$  will be larger than the number of components of the  $\mathbf{F}$  function  $m$ , the system [4] will in general be underdetermined. Therefore, the problem has infinite solutions, and some criterion is needed to chose a specific one. In this study, a solution is chosen arbitrarily, simply selecting the one obtained when solving [4] using the least-square method (more explicitly, the system is solved using the LAPACK<sup>[48]</sup> function `dgelsd` from Numpy). The introduction of additional constraints would further reduce the number of possible solutions.

A new texture is then found applying a small change in the direction defined by the solution of [4]:

$$\mathbf{C}' = \mathbf{C} + k\Delta\mathbf{C} \quad [5]$$

The factor  $k$  in [5] is defined differently in distinct variations of the gradient descent method. Some of the most advanced algorithms determine which is the largest trust region in which the estimation of the gradient can be considered valid in order to achieve the fastest convergence. In the case under consideration, fast convergence is not desirable, because the goal of the method is not only to find the optimum values but, more importantly, to determine how to gradually modify an existing texture to approach that optimum. To generate a large number of intermediate steps, the value of  $k$  will be chosen such that the total relative variation in the C-coefficients does not exceed a limit value  $K$ , *i.e.*,  $k$  is chosen such that:

$$\frac{k \sum_i \Delta C_i}{\sum_i C_i} < K \quad [6]$$

The set of C-coefficients  $\mathbf{C}'$  given by [5] does not necessarily correspond to a valid ODF because of the possible appearance of negative values. Therefore, if the minimum value of the ODF is lower than a defined limit, the ghost correction method described in Section II-A will be applied until the desired conditions are met. An additional advantage of using a ghost correction method is that it allows limiting the solution space to the even C-coefficients of the ODF series expansion, such that the solution space corresponds with the different measurements that can be performed using XRD techniques, whereby only the even part of the ODF can be reconstructed from pole figures and odd coefficients are calculated using ghost correction. Consequently, it will be necessary to evaluate the objective function for a total of  $n + 1$  different ODFs, where  $n$  is the number of independent even C-coefficients in the ODF (125 in the common case of  $l = 22$  and orthorhombic symmetry).

After the ghost correction method has been applied, a new texture that produces a lower value of the objective function is obtained. Another run of the method can be performed on this new texture until a minimum is reached or some other stop criterion is met.

### C. Texture Optimization for Improved Formability

In this work, texture will be optimized for improved sheet formability. The objective function is defined as a function of two components: one is related to the average of the  $q$  values  $\mu_q$  and the other to its standard deviation  $\sigma_q$ :

$$\mathbf{F}(\mathbf{C}) = \begin{bmatrix} \mathbf{w}(1 - \mu_q(\mathbf{C})) \\ (1 - \mathbf{w})\sigma_q(\mathbf{C}) \end{bmatrix} \quad [7]$$

The factor  $w$  is a weight that varies depending on the distance to the objective and a selected tolerance, and if the solution is converging or diverging. The values  $\mu_q$

and  $\sigma_q$  are calculated using the  $q$  values given by the method described in Section II–D and the equations defined in [1].

An optimization step will consist on first evaluating the function  $F$  with the initial C-coefficients calculating the  $q$  values using the Taylor model (see Section II–D) and the corresponding  $\mu_q$  and  $\sigma_q$  magnitudes with [1]; estimate the gradient using [3], which will have two components, one relative to  $\mu_q$  and the other to  $\sigma_q$ , both of them defined as a function of the Euler angles, and then solving the linear system in [4]; applying the ghost correction method if the minimum value of the ODF is lower than the 10 pct of its maximum, and, finally, calculating new C-coefficients using [5] and [6], such that the variation with respect to the previous ones is not larger than 10 pct (*i.e.*,  $K = 0.1$ ). This entire process is represented in Figure 1.

#### D. Prediction of $q$ Values Based on the Full Constraints and Relaxed Taylor Theory

The  $q$  values corresponding to a given texture and crystal structure are calculated using a crystal plasticity model. The Taylor assumption will be applied, which considers that the strain in every material point is equal to the macroscopic one. Furthermore, some criterion is needed to know which of the possible slip planes are activated to accommodate deformation. The Bishop-Hill theory<sup>[17,49]</sup> gives a partial solution of the problem under the hypothesis that the slip planes activated are those that minimize the total energy. An additional condition is needed to obtain a unique solution. The criterion followed is to choose the solution that minimizes not only the energy, but also its derivative.<sup>[50]</sup>

In addition to the full constraints Taylor assumption, the relaxed constraints case will be considered.<sup>[51]</sup> Relaxations are introduced in the model adding additional degrees of freedom in the form of “pseudo-slip

systems” with a critical resolved shear stress of zero. For instance, the “pancake” model, in which it is assumed that grains have a pancake-like shape parallel to the sheet and therefore deform freely in shear along normal planes, defines two additional pseudo-slip systems:

$$\mathbf{K}_{m+1}^s = \begin{bmatrix} 001 \\ 000 \\ 000 \end{bmatrix} \quad \mathbf{K}_{m+2}^s = \begin{bmatrix} 000 \\ 001 \\ 000 \end{bmatrix} \quad [8]$$

The implementation of the models used in this study will again be the one found in the MTM-FHM software package, where the  $q$  values are calculated using a precomputed solution of the Taylor–Bishop-Hill problem in the form of a series expansion of Taylor factors for each possible combination of loading direction in the sheet plane and contraction ratio (such that 21 equispaced values in the domain  $0 \leq q \leq 1$  are considered for each loading direction). Once a database with all the possible Taylor factors has been built, it is possible to find the  $q$  values for any texture and loading direction in a very efficient way. Further details can be found in the software manual<sup>[45]</sup> and Reference 13.

### III. OPTIMIZATION OF BCC AND FCC TEXTURES

The method presented in the previous section is applied to several textures typical for the FCC and BCC rolled sheets that are employed for press-forming operations in automotive products, whereby deep drawability is of crucial importance.

The ODFs of all the initial textures are shown in Figure 2. It is observed that the BCC1 and BCC2 textures (Figure 2(a)) are typical for a cold-rolled BCC material, with a strong  $\gamma$  fiber and also some intensity

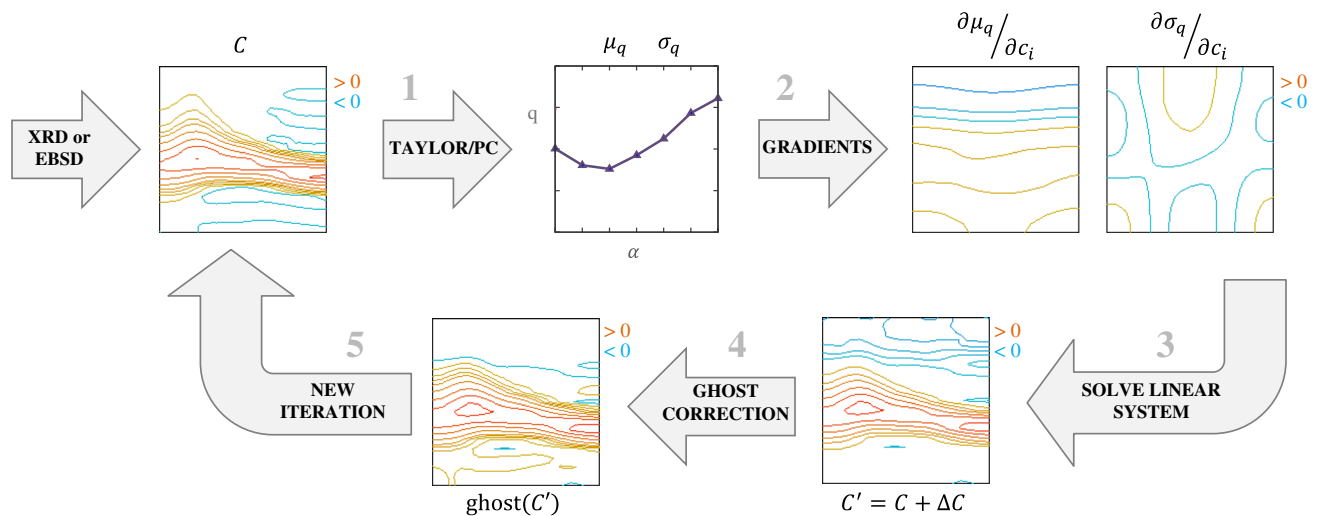


Fig. 1—Optimization algorithm: starting with an initial texture, the initial  $\mu_q$  and  $\sigma_q$  values are calculated (1), as well as their gradients with respect to texture components (2), and used to find the direction of maximum descent and a new texture in that direction (3). Finally, the ghost correction method is applied if needed (4), before proceeding to a new iteration (5).

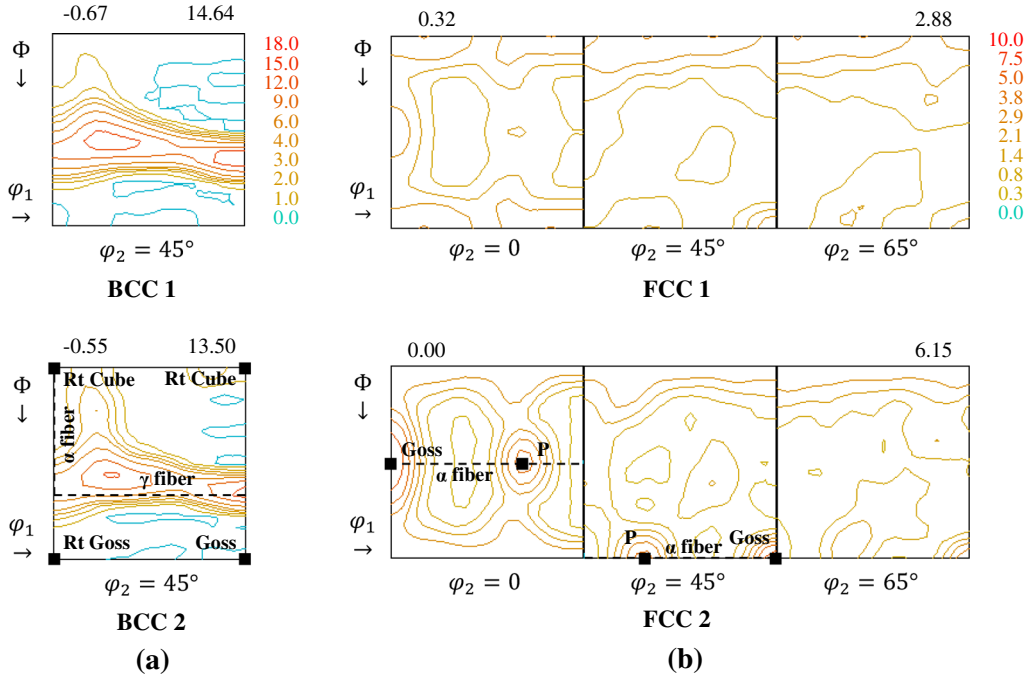


Fig. 2—Selected sections of the ODFs of the initial textures: (a) BCC textures ( $\varphi_2 = 45$  deg section). (b) FCC textures (sections at  $\varphi_2 = 0, 45$  and  $65$  deg). On top, the minimal and maximum values of the ODF are displayed.

along the  $\alpha$  fiber, specially in BCC2, which also shows a higher intensity around the rotated cube component. FCC textures [Figure 2(b)], on the other hand, show strong Goss and P components, characteristic of a material subjected to recrystallization in an annealing process after cold rolling.

Figure 3 shows the  $q$  values predicted for the initial textures using different sets of slip systems, while Table I shows the average and standard deviation for each case. Table I additionally lists the values for a randomly textured polycrystal. For BCC textures, either two systems,  $\{110\}\langle 111 \rangle$  and  $\{112\}\langle 111 \rangle$ , or also a third one,  $\{123\}\langle 111 \rangle$ , are considered, in both the full constraints (Taylor) and relaxed constraints (pancake) models. In the case of FCC textures, the only slip system considered is  $\{111\}\langle 110 \rangle$ , again using the Taylor and pancake models.

Some differences are observed depending on the model used, particularly in the case of BCC textures. However, the effect of the additional slip system is quite limited. Indeed, although the  $q$  values obtained are larger when using three slip system families, their variation with the angle is similar to the two slip system families case. Due to the small differences observed, in the following only two slip systems will be considered<sup>†</sup>.

<sup>†</sup>This decision is arbitrary. In practice, two or three slip systems would be chosen depending on which one better approximates the experimental results.

In addition to the rolled sheet textures just presented, random BCC and FCC textures are studied. In a random texture, all the orientations have equal probability and, therefore, the ODF is a constant function. When the Taylor model is used, a random texture will show an isotropic behavior independently of its crystal structure, which means that transversal and normal strains are always equal to half the longitudinal one and therefore:

$$q_{rnd,x} = 0.5 \forall \alpha \Rightarrow \mu_q = 0.5, \sigma_q = 0 \quad [9]$$

However, when the pancake model is used, some anisotropy is introduced because the orientation of the additional slip systems, introduced to provide extra degrees of freedom, is defined based on the orientation of the plate and not the crystallographic orientation, which is the case for conventional slip systems. Therefore, in this case,  $\mu_q$  only reaches 0.433 for BCC and 0.465 for FCC, as can be seen in Table I.

### A. Formability Gradient Distribution Function

The gradient of the  $\mu_q$  and  $\sigma_q$  values with respect to the C-coefficients is estimated using the method described in the previous sections: given an initial texture, a small perturbation  $\Delta c$  is applied to each coefficient (see Figure 4), and the  $q$  values calculated with a crystal plasticity model are compared with those of the initial texture. As discussed before, it is necessary

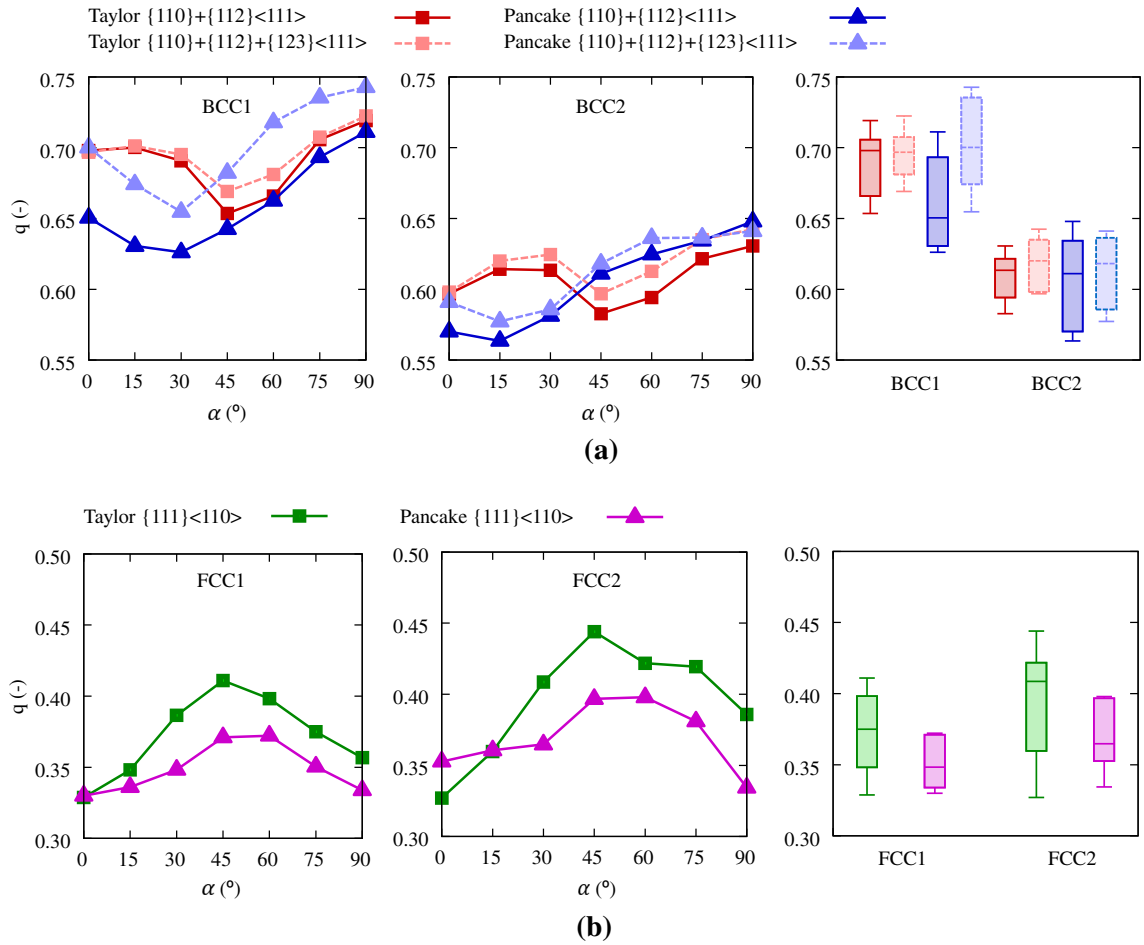


Fig. 3—Initial  $q$  values of the (a) BCC and (b) FCC textures in Fig. 2, calculated for seven different directions between 0 and 90, at 15-degree intervals. At right, a box plot showing the quartiles and limits for each model. See also Table I.

Table I. Average and Standard Deviation of the  $q$  Values of the Initial (a) BCC and (b) FCC Textures

Material	Taylor				Pancake			
	{110}+{112}		{110}+{112}+{123}		{110}+{112}		{110}+{112}+{123}	
	$\mu_q$	$\sigma_q$	$\mu_q$	$\sigma_q$	$\mu_q$	$\sigma_q$	$\mu_q$	$\sigma_q$
(a)								
BCC1	0.687	0.006	0.656	0.008	0.694	0.004	0.698	0.009
BCC2	0.607	0.004	0.604	0.008	0.618	0.004	0.611	0.007
BCCrnd	0.500	0.000	0.500	0.000	0.434	0.000	0.433	0.000
(b)								
	Taylor		Pancake					
Material	$\mu_q$	$\sigma_q$	$\mu_q$	$\sigma_q$				
FCC1	0.377	0.007	0.352	0.004				
FCC2	0.402	0.010	0.374	0.006				
FCCrnd	0.500	0.000	0.465	0.000				

See also Fig. 3

to find a value for  $\Delta c$  that is neither too large or too small. After some preliminary trials, it was decided to use a value of  $\Delta c = 0.01$  for every gradient calculation, independently of the crystal structure and plasticity

model used. This decision will be further discussed in Section IV-C.

Figures 5 and 6 show the distribution functions of the gradients of the average and standard deviation of the

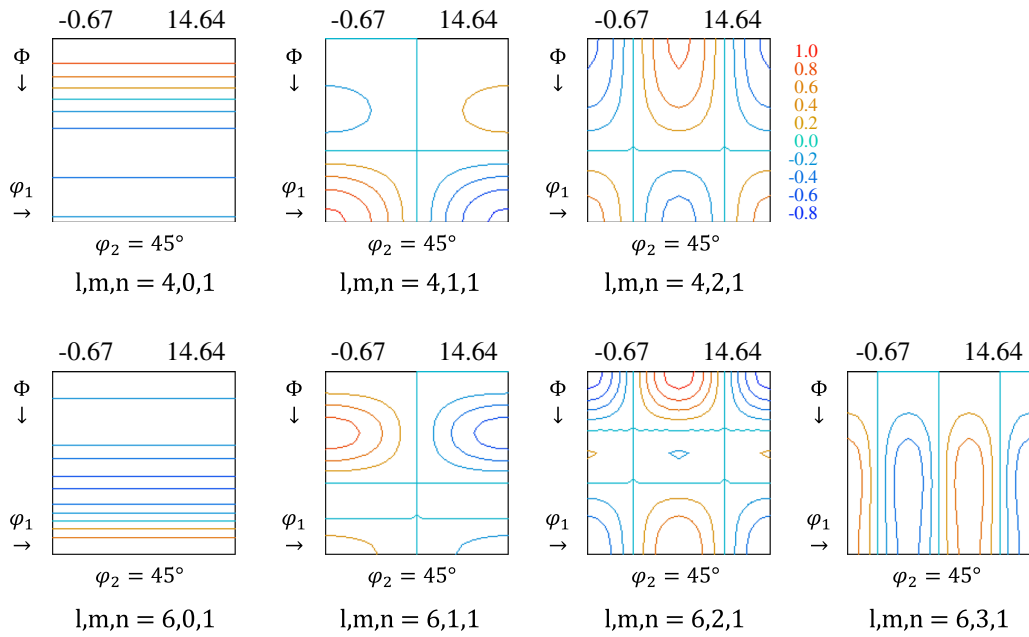


Fig. 4—Perturbation applied to the initial texture corresponding to the first seven even C-coefficients (for  $\Delta c = 1$ ). Maximum and minimum values are displayed on top.

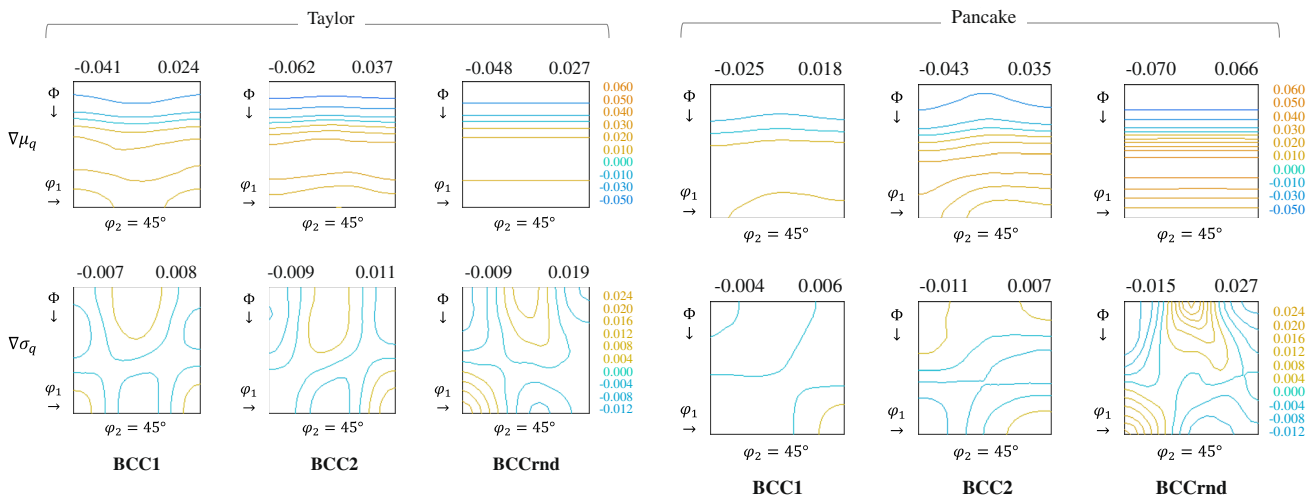


Fig. 5—Initial gradient distribution function of the average  $q$  values ( $\mu_q$ ) and their standard deviation ( $\sigma_q$ ) for the textures in Figure 2 using the Taylor and pancake models, calculated using  $\Delta c = 0.01$ . Maximum and minimum values are displayed on top.

predicted  $q$  values for the initial BCC and FCC textures, respectively. Since the gradient is calculated with respect to every coefficient, the rate of change of the formability indicators is defined for every orientation in the Euler space and can therefore be represented as a distribution function using the harmonic series expansion method, analogous to an ODF. Figure 5 shows that, in all cases, texture components in the  $\varphi_2 = 45$  degree section with  $\Phi > 30$  degrees increase the  $\mu_q$  value, while for  $\Phi < 30$  degrees it decreases. The gradient is less pronounced for BCC1, since higher initial  $q$  values (see previous section) offer fewer possibilities of improvement. There are some slight differences depending on which plasticity model is used, but they all show very similar trends. When

observing the standard deviation gradients, it is seen that the components along the  $\gamma$  fiber always exhibit a negative value (therefore reduce anisotropy on the sheet plane), as could be expected. Other components increase or reduce the standard deviation value depending on the intensity of the initial texture.

It may seem counterintuitive that negative values are present in the  $\sigma_q$  gradient of random textures. Indeed, since the initial value is zero and, by definition, the standard deviation is positive, the initial gradient should also be  $\geq 0$  for every orientation. The appearance of negative values is again an artifact resulting from approximating the function using a finite series. However, since for  $\sigma_q = 0$  the weight given to the standard

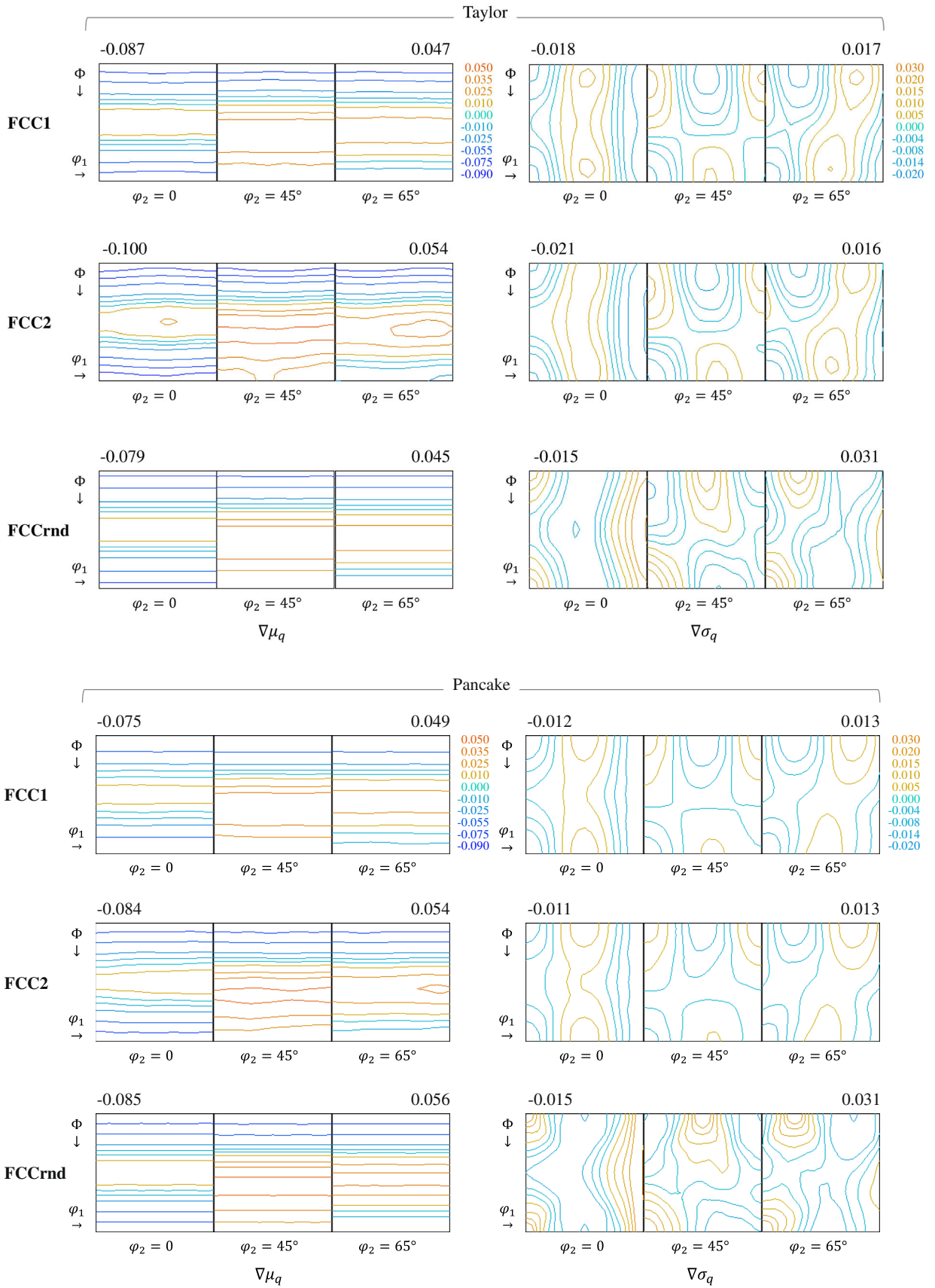


Fig. 6—Initial gradient distribution function of the average  $q$  values ( $\mu_q$ ) and their standard deviation ( $\sigma_q$ ) for the textures in Fig. 2(b) and the random FCC texture using the Taylor and pancake models, calculated using  $\Delta c = 0.01$ . Maximum and minimum values are displayed on top.

deviation equation in [7] will be zero, this inaccuracy will not affect the results.

In the case of FCC textures, shown in Figure 6, it is observed that both plasticity models yield very similar results for  $\mu_q$  and  $\sigma_q$  gradients.

### B. Optimized Textures

Using the gradients, a new texture with better formability properties can be obtained applying the described method. Figure 7 shows the results of applying this method to different initial textures of commercially available sheet products iteratively, for a total of 500 optimization steps using a  $K$  value (see Eq. [6]) of 0.1. In the graph, the evolution of  $\mu_q$  and  $\sigma_q$  is represented with respect to the average variation of the ODF, measured using a discretization of the texture in the Euler space at 5-degree intervals, such that:

$$\text{var} = \frac{1}{n_1 \cdot n \cdot n_2} \sum_{\varphi_1} \sum_{\Phi} \sum_{\varphi_2} (g_N(\varphi_1, \Phi, \varphi_2) - g_0(\varphi_1, \Phi, \varphi_2)) \quad [10]$$

where  $g_0(\varphi_1, \Phi, \varphi_2)$  is the initial ODF,  $g_N(\varphi_1, \Phi, \varphi_2)$  the optimized texture for step  $N$ , and  $n_1$ ,  $n$  and  $n_2$  are the number of values for  $\varphi_1$ ,  $\Phi$  and  $\varphi_2$ , respectively (with a step of 5 degrees and orthorhombic symmetry,  $n_1 = n = n_2 = 17$ ).

Figure 7 shows that, as was the objective, formability properties are improved. While  $\mu_q$  approaches (although does not reach) the optimal value of one,  $\sigma_q$  is reduced and kept below the prescribed tolerance of 0.001. The

graphs show that, for all the textures with the same crystal structure, the rate at which  $\mu_q$  increases is almost constant for both plasticity models, until it reaches a plateau, corresponding to a local equilibrium point. The final value obtained is different for each texture, showing that the equilibrium point is indeed a local optimum, as can be expected from a gradient descent method. The  $\sigma_q$  value also decreases in a similar way in every case. However, when BCC textures are optimized, a change of slope is observed, such that after a relatively slow decrease, there is a sudden reduction until levels below tolerance are reached.

Figure 8 shows that both the Taylor and pancake models produce very similar textures. The optimized BCC textures progressively become sharper than the original ones, specially around the  $\gamma$  fiber, which becomes considerably stronger. During the first part of the optimization, most of the components far away from this fiber are weakened until the components with low  $\Phi$  values disappear. From this point, which approximately corresponds to the change of slope in the  $\sigma_q$  graph in Figure 7(a), the  $\gamma$  fiber becomes more uniform over  $\varphi_1$ , better approaching an ideal fiber. Section IV-D will further discuss the evolution of the  $\gamma$  fiber components during the optimization process.

Figure 9 shows the evolution of the FCC textures. Also in this case, the differences between the results obtained with the two plasticity models are hardly noticeable. Similar to BCC textures, all the studied FCC textures become sharper during the optimization. Eventually, most of the components far away from the  $\alpha$  fiber are reduced until they almost disappear, and the Goss

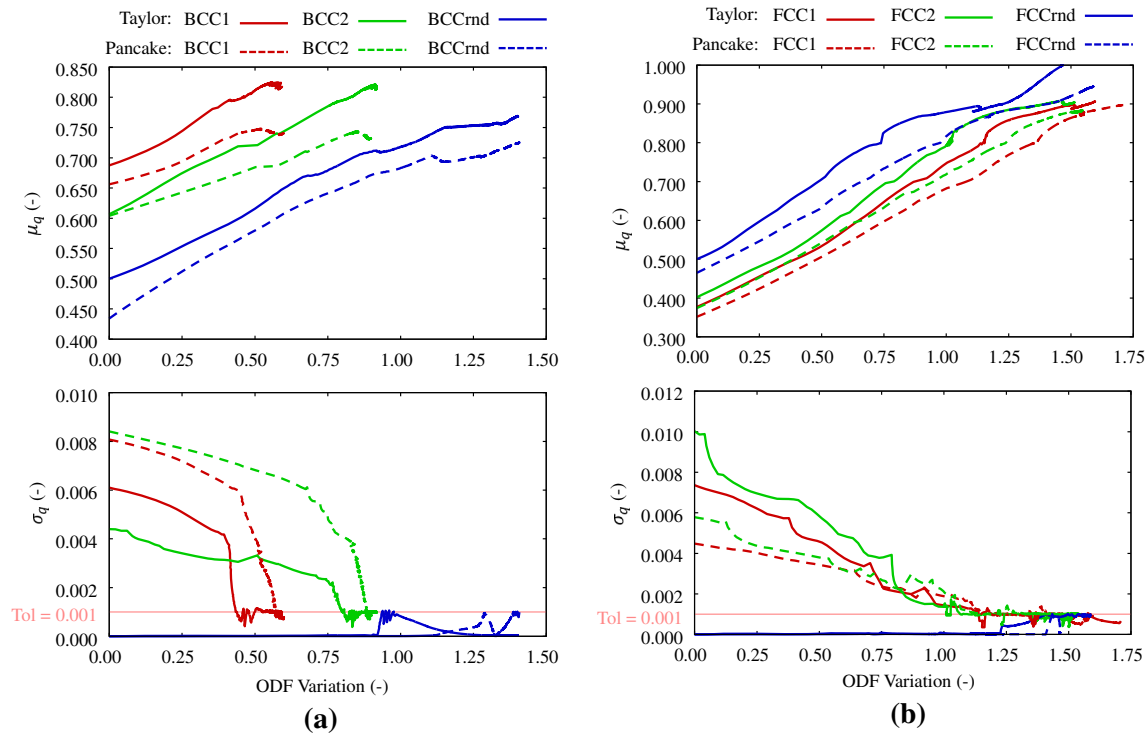


Fig. 7—Evolution of average and standard deviation of  $q$  values for (a) BCC and (b) FCC textures with respect to ODF variation.

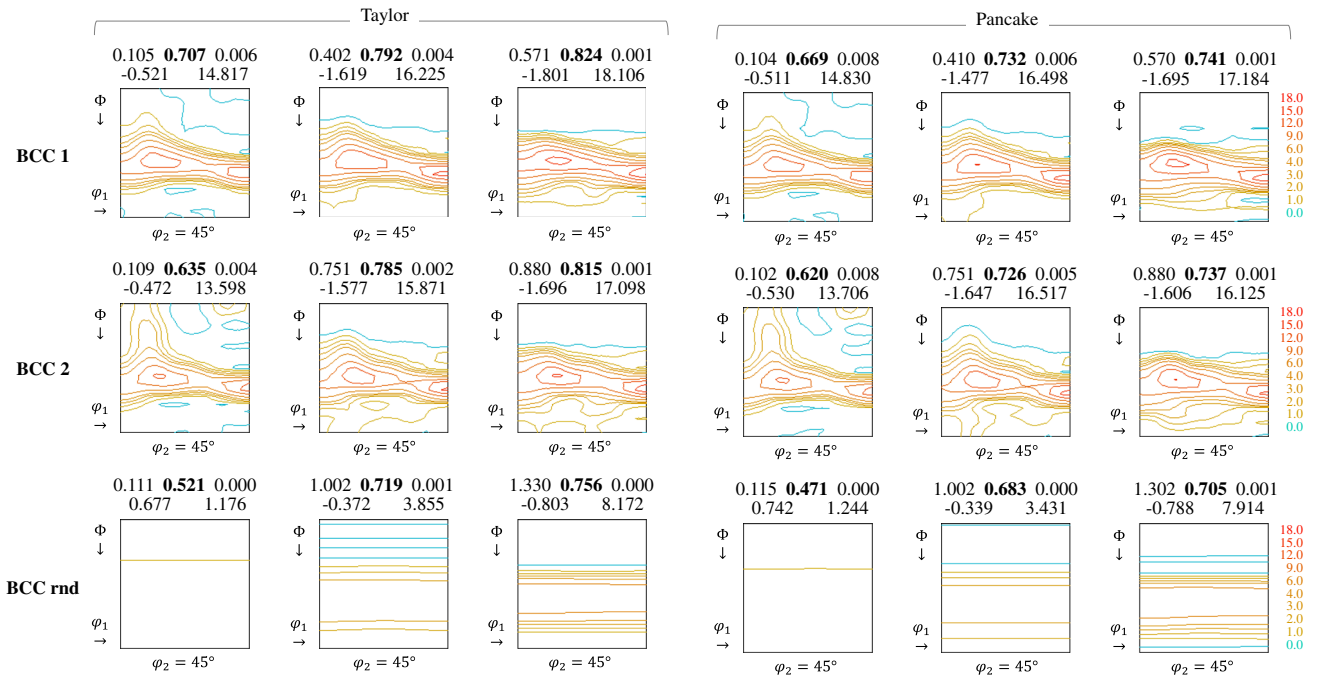


Fig. 8—BCC textures obtained during the optimization process. On top, the variations of the ODF [see (10)],  $\mu_q$  (in bold) and  $\sigma_q$ , corresponding to each texture, are displayed on the first line and the maximum and minimum values on the second one. For each case, the ODF sections corresponding to three different instants of the optimization are shown: at the beginning of the process, the approximate middle and the end of the process.

and P components, which were already dominant in the FCC1 and FCC2 textures, become even stronger. It is remarkable that, while a very uniform fiber is obtained when optimizing a random texture, the optimized FCC1 and FCC2 textures (particularly the latter) show stronger Goss and P components, as in the corresponding original textures. The different results are once more a consequence of using a method that finds local minima. Nevertheless, in all cases the  $q$  values are significantly improved.

## IV. DISCUSSION

### A. Local Minima

The texture optimization method presented is based on the gradient descent algorithm and therefore is only capable of finding local minima, but not global ones. Initially, it is assumed that producing the textures corresponding to local minima will already suppose a challenge for the industry, and therefore there is not an urgent need to find global optima with even better properties. However, this assumption must be verified, checking that the solutions found indeed represent a significant improvement.

Observing the results from the previous section, it is obvious that the optimal textures found effectively show a pronounced increment in formability, and therefore the results obtained can be applied to the improvement of industrial processes. Nevertheless, as previously said

in the introduction, it must be noted that the method presented may be easily extended to also search for global minima, for example, using some randomization of the solution using the temperature concept of simulated annealing algorithms. This approach may be preferable when additional constraints are introduced in the problem.

In industrial applications, it is generally known which theoretical textures are needed to obtain optimum properties. However, reaching these textures with actual techniques is not an option. To modify current processes, the industry wants to know how to achieve the maximum improvement with minimum changes. A gradient descent optimization provides exactly this information. For example, Figure 10 shows the first increment of the optimization (using the Taylor model) for the three BCC textures. Although all the textures reach a similar optimum (see Figure 8), close to a gamma fiber, and the BCC1 and BCC2 textures were very similar [Figure 2(a)], there are subtle differences in the increments shown in Figure 10. Knowing that modifications to an existing texture should approach the results from Figure 10 is more useful information than the knowledge of an unreachable optimum texture.

### B. Crystal Plasticity Model

It was already well known, as mentioned in the introduction, that the Taylor and pancake models give different predictions of  $q$  values. Similar results are

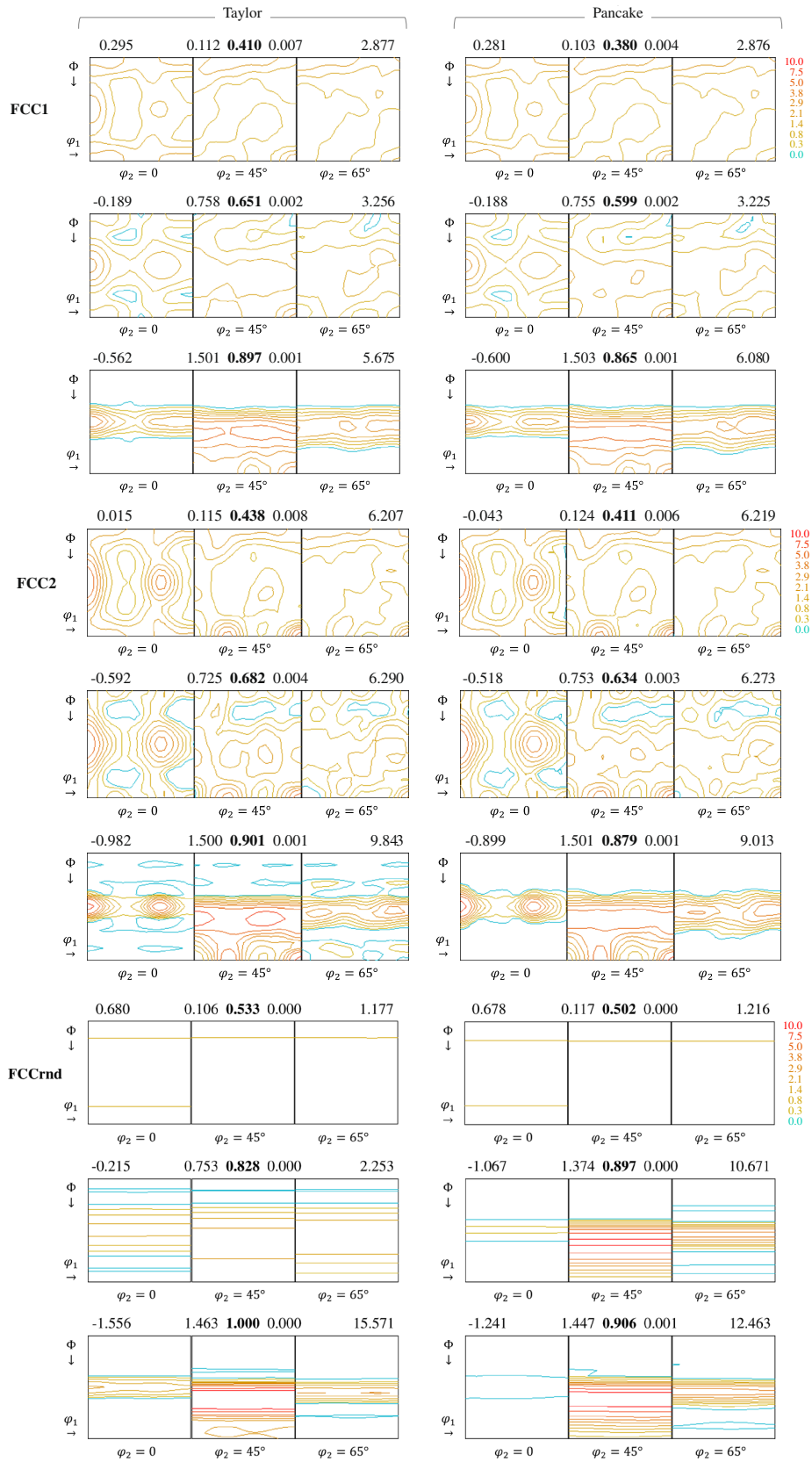


Fig. 9—FCC textures obtained during the optimization process. On top, the variation of the ODF [see equation [10]],  $\mu_q$  (in bold) and  $\sigma_q$ , corresponding to that texture, as well as the maximum and minimum values. For each case, the ODF sections corresponding to three different instants of the optimization are shown: at the beginning of the process, the approximate middle and the end of the process.

obtained in this study. Indeed, Figure 3 shows that, in general, the Taylor model returns slightly higher  $\mu_q$  values. There are also appreciable differences in the variation of the values with respect to  $\alpha$ . While for FCC materials both models give a similar trend but with higher  $\sigma_q$  values using the Taylor model, for BCC textures the pancake model gives higher standard deviation. Moreover, although the highest  $r$  value is

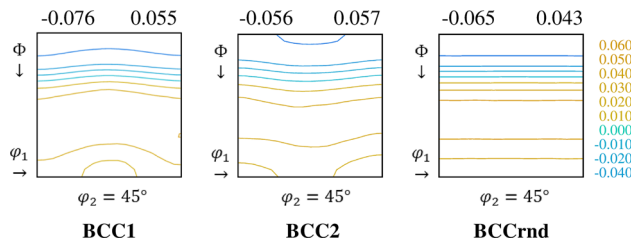


Fig. 10—Increment with respect to the original textures in Fig. 2(a) after the first optimization step from Section III using the Taylor model.

always found at 90 deg with respect to the rolling direction, the minimum is found at lower  $\alpha$  values using the pancake model.

Despite these differences, the gradients presented in Figures 5 and 6 are very similar independently of the model used, specially the  $\mu_q$  gradient. There are some differences observed in the gradient of  $\sigma_q$  but, as can be seen in Figures 8 and 9, the obtained textures for an equivalent variation of the ODF are actually almost identical.

It remains to be studied how the method would behave using other plasticity models, as, for example, the ALAMEL<sup>[52]</sup> or VPSC<sup>[53]</sup> models. However, the larger complexity of these models makes them much less suitable for its usage in an iterative method as the one presented here, where the spectral technique used to solve the Taylor–Bishop–Hill theory offers an exceptionally high performance. Nevertheless, it is possible to considerably speed up the optimization process performing different simulations in parallel. Moreover, it can be presumed that using more elaborated models will become a feasible option with further advancements in

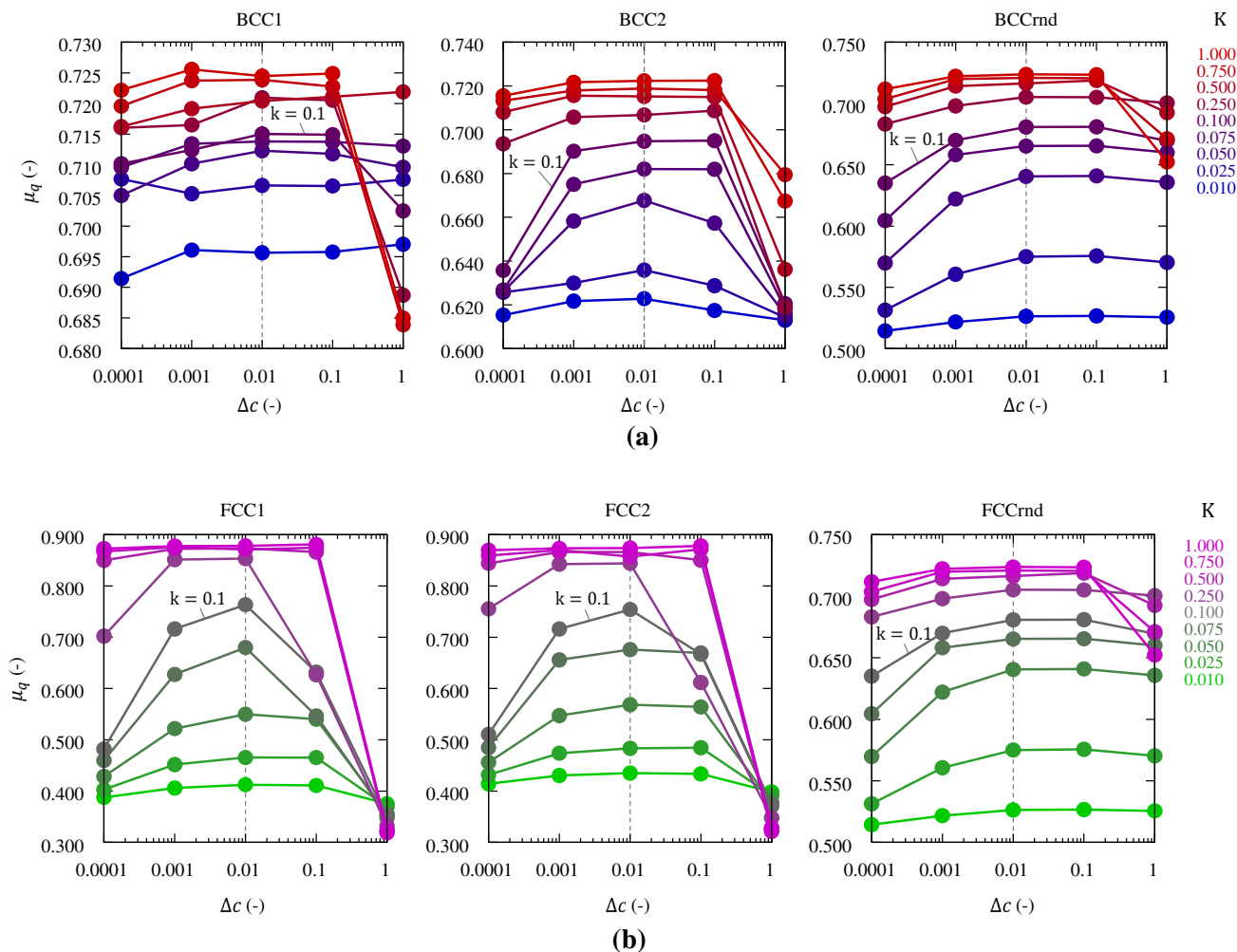


Fig. 11—Value of  $\mu_q$  obtained for  $k = 0.01, 0.025, 0.050, 0.075, 0.1, 0.25, 0.50, 0.75, 1$  and  $\Delta c = 0.0001, 0.001, 0.01, 0.1, 1$  after 50 optimization steps for (a) BCC and (b) FCC textures.

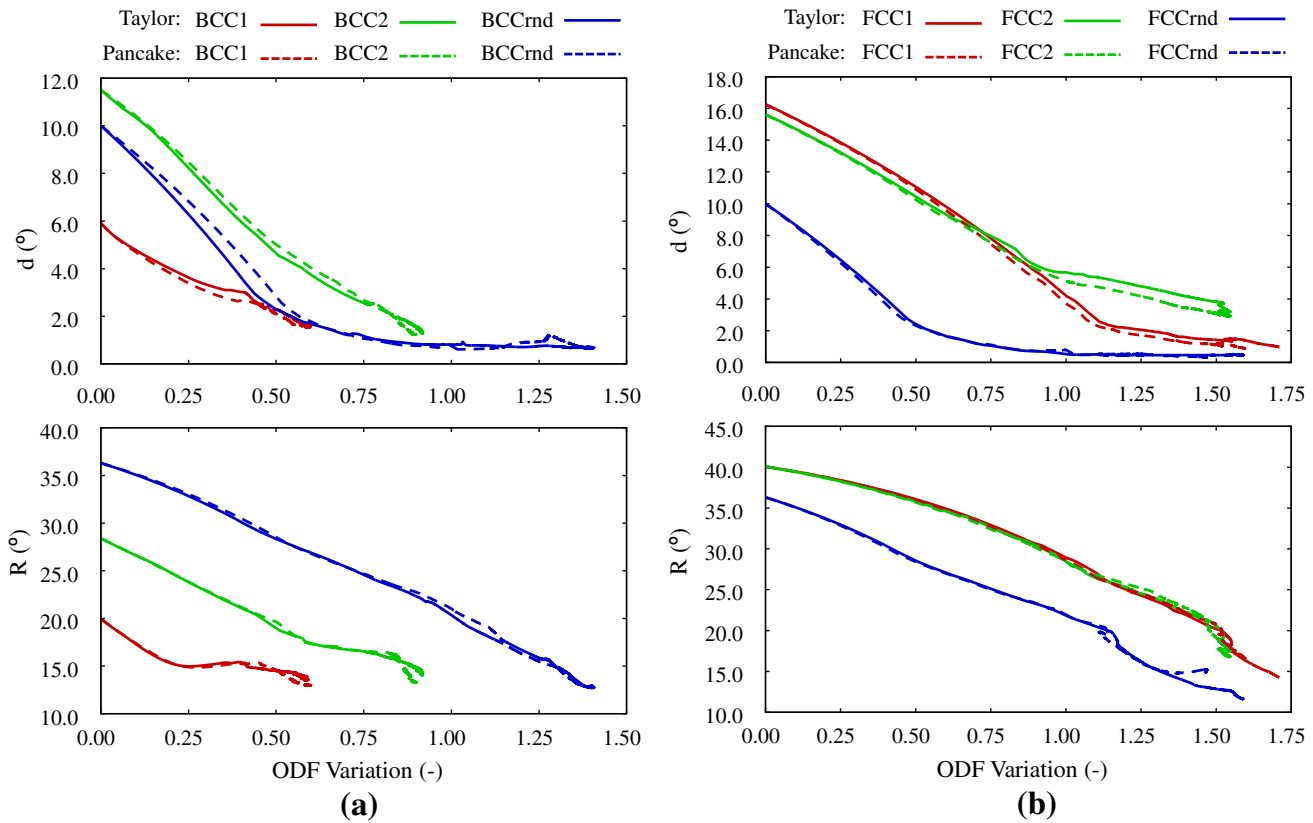


Fig. 12—Evolution of the radius of the skeleton line  $R$  and its distance to the  $\gamma$  fiber  $d$  during the optimization of the (a) BCC and (b) FCC textures.

computing capacity<sup>‡</sup>. Therefore, this option is already

<sup>‡</sup>The Taylor method was also considered prohibitively computationally expensive not so long ago,<sup>[15]</sup> but nowadays it can be solved almost instantly by a standard computer.

being investigated and currently is a work in progress.

### C. Choice of Optimization Parameters

In Sections III–A and III–B, the optimization parameters  $\Delta c$  and  $K$  were set to the values 0.01 and 0.1, respectively. The  $\Delta c$  value, defined in Eq. [3], defines the perturbation applied to estimate the gradient, while  $K$ , defined in [5], limits the relative change between consecutive optimization steps. This section discusses in more depth the validity of the chosen values. With this goal, 50 optimization steps are performed using all the BCC and FCC textures for different  $k$  values ranging from 0.01 to 1.0 and  $\Delta c$  values from 0.0001 to 1.0.

Figure 11 shows the  $\mu_q$  value obtained for each case using the Taylor model (analogous results are obtained for  $\sigma_q$  and using the pancake model, not shown in the figure). As can be seen, in general the highest  $\mu_q$  values are obtained for  $0.001 < \Delta c < 0.1$ . Moreover, the  $q$  values obtained are comparatively insensitive to the variation of  $\Delta c$  in this range. Therefore,  $\Delta c = 0.01$  indeed appears to be a sensible value for the calculation of gradients, at least for the textures considered in this study.

When the results for different values of  $K$  are considered, it is seen that the optimization can be performed in fewer steps using values higher than the selected one of 0.1. Indeed, the graphs show that, for a fixed number of optimization steps, the best formability is obtained for the value  $K = 1.0$ . Therefore, if it were desired to achieve convergence as fast as possible, it would be advisable to increase the value of  $K$ . However, in this case, it is considered that a lower value is preferable, because it will produce a higher number of intermediate textures, making easier to analyze and compare the obtained results. Evidently, this decision will imply that a higher number of iterations is needed to reach a given objective.

### D. Comparison of Obtained Textures with Ideal $\gamma$ Fiber Texture

As shown in Section III–B, all the textures progressively develop a stronger  $\gamma$  fiber during the optimization process. In this section, the textures are compared with an ideal  $\gamma$  fiber texture in a quantitative way, using the method described in the Appendix.

The evolution of the  $d$  and  $R$  values during the optimization process is shown in Figure 12. The figure clearly shows that the distance to the  $\gamma$  fiber, as well as the radius of the fiber textures, consistently decreases as the formability properties are improved. This is also observed when looking at the equivalent

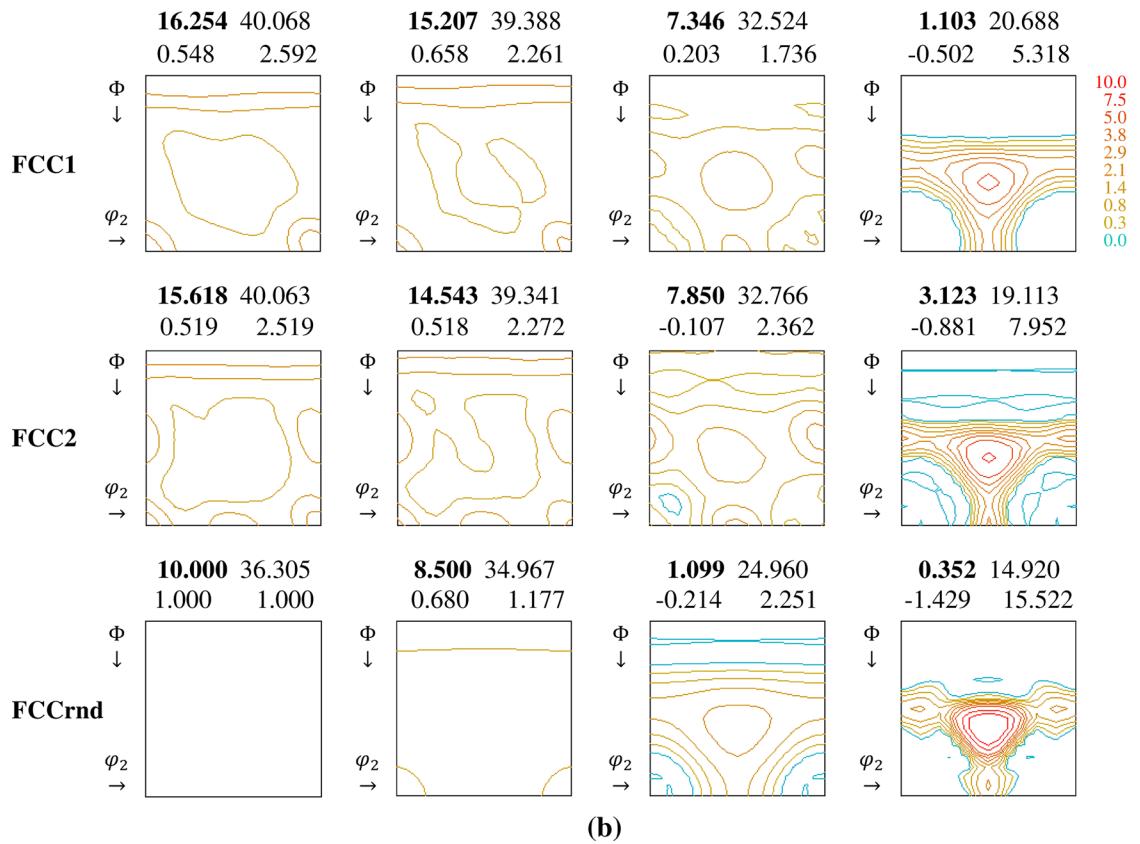
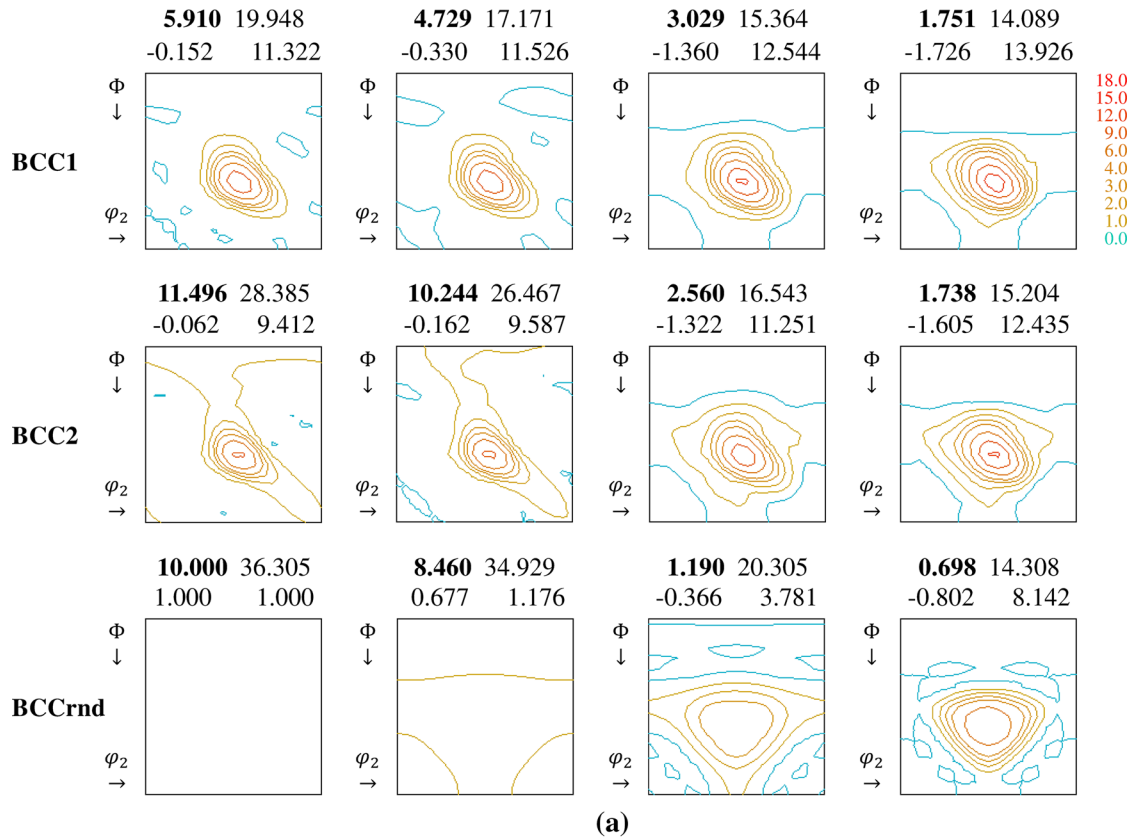


Fig. 13—Obtained BCC (a) and FCC (b) fiber textures. On top, the corresponding distance to the ideal  $\gamma$  fiber  $d$  (in bold) and the radius of the fiber texture  $R$ .

fiber textures obtained from the textures in Figures 8 and 9, which are displayed in Figure 13.

Figure 13 also shows additional details about the topology of the obtained fiber texture and its evolution during the optimization process. In particular, the figure shows that, while for BCC textures the fiber texture consistently becomes more concentrated, in the case of FCC materials there also are some weaker components outside of this fiber (for approximately  $\Phi = 54$  deg and  $\varphi_2 = 45$  deg,  $\Phi < 54$  deg), distributed symmetrically with respect to  $\varphi_2 = 45$  deg.

## V. CONCLUSIONS

A new optimization method for the improvement of the formability properties of crystallographic textures has been presented. The method, based on the gradient descent algorithm, makes use of a linear estimation of the gradient of the average and standard deviation of the  $q$  values predicted by the Taylor model to find a local minimum. Although the optimal textures, corresponding to a strong  $\gamma$  fiber, were already well known, the added value of the method is that it provides a path of incremental changes toward an optimal solution in the most efficient way.

The method has been applied to the optimization of several BCC and FCC textures, corresponding to typical sheet products and an ideal random texture. It has been shown that the textures obtained indeed offer better formability as predicted by the model, with significantly higher and more uniform  $q$  values, than the original ones. As was expected, optimizing the textures involves a reinforcement of the components closer to the ideal  $\gamma$  fiber.

Although the obtained results do not offer many novelties in terms of the description of the optimum texture, as it was already known that the textures with the strongest  $\gamma$  fibers would have better formability, the method shows that the calculation of a gradient based in a crystal plasticity model is an useful tool for the identification of components with the potential to improve formability. Therefore, the optimization

method developed may be used as the basis for more complicated studies, in which a similar gradient of the variation of texture components with respect to processing parameters is used for the optimization of specific materials and production processes.

## ACKNOWLEDGMENTS

This work has been carried out in the framework of the BaseForm project. This project has received funding from the European Unions Research Fund for Coal and Steel (RFCS) research program under grant agreement #RFCS-CT-2014-00017. The authors would also like to thank Tata Steel, and in particular Jaap Moerman and Stefan Van Bohemen, as well as Ghent University, for providing the initial textures used in this study and very insightful discussion.

## OPEN ACCESS

This article is distributed under the terms of the Creative Commons Attribution 4.0 International License (<http://creativecommons.org/licenses/by/4.0/>), which permits unrestricted use, distribution, and reproduction in any medium, provided you give appropriate credit to the original author(s) and the source, provide a link to the Creative Commons license, and indicate if changes were made.

## APPENDIX

### *A Equivalent Fiber Texture and Comparison with Ideal $\gamma$ Fiber Texture*

This Appendix describes how to calculate, for a generic texture, an equivalent fiber texture, consisting only of a single and homogeneous (constant radius) fiber parallel to the  $\phi_1$  direction in the Euler space and how to

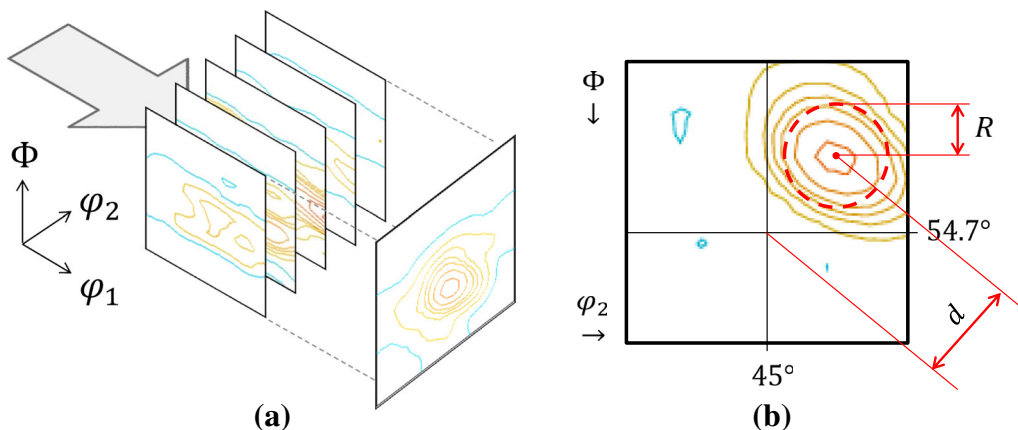


Fig. A1—Schematic diagram of the calculation of fiber textures integrating over  $\varphi_1$  (a) and the  $d$  and  $R$  magnitudes (b), corresponding to the distance to the  $\gamma$  fiber at  $\varphi_2 = 45$  deg and  $\Phi = 54.7$  deg and the radius of the fiber texture.

compare this equivalent texture with an ideal  $\gamma$  fiber texture.

The calculation of the equivalent texture is performed in two steps. First, the  $g(\varphi_1, \Phi, \varphi_2)$  texture is converted, after discretization on a 5-degree grid, to an equivalent  $g'(\Phi, \varphi_2)$  texture consisting of fibers parallel to  $\varphi_1$  (Figure A1(a)), such that:

$$g'(\Phi, \varphi_2) = \frac{1}{n_1} \sum_{\varphi_1} g(\varphi_1, \Phi, \varphi_2) \quad [\text{A1}]$$

where  $n_1$  is the number of  $\varphi_1$  values (with a step of 5 deg and orthorhombic symmetry,  $n_1 = 17$ ). Then,  $g'$  is converted to a texture consisting of a single fiber with center  $(\varphi'_2, \Phi')$  and radius  $R$ , calculated as:

$$(\varphi'_2, \Phi') = \left( \frac{\sum_{\Phi} \sum_{\varphi_2} g'(\Phi, \varphi_2) \varphi_2}{\sum_{\Phi} \sum_{\varphi_2} g'(\Phi, \varphi_2)}, \frac{\sum_{\Phi} \sum_{\varphi_2} g'(\Phi, \varphi_2) \Phi}{\sum_{\Phi} \sum_{\varphi_2} g'(\Phi, \varphi_2)} \right) \quad [\text{A2a}]$$

$$R = \frac{\sum_{\Phi} \sum_{\varphi_2} g'(\Phi, \varphi_2) \sqrt{(\varphi_2 - \varphi'_2)^2 + (\Phi - \Phi')^2}}{\sum_{\Phi} \sum_{\varphi_2} g'(\Phi, \varphi_2)} \quad [\text{A2b}]$$

Once the equivalent single-fiber texture has been calculated, it can be compared with an ideal  $\gamma$  fiber texture. This ideal fiber is defined as parallel to  $\varphi_1$  with  $\varphi_2 = 45$  deg and  $\Phi = 54.7$  deg. The ideal and calculated textures are compared using two parameters: the first one is the radius of the calculated texture  $R$ , given by [A2b], which will approach zero as the calculated texture becomes closer to an ideal one; the second parameter is the distance  $d$  from the center of the calculated fiber, given by [A2a], and the center of the ideal texture [see Figure A1(b)], such that:

$$d = \sqrt{(\varphi'_2 - 45)^2 + (\Phi' - 54.7)^2} \quad [\text{A3}]$$

## REFERENCES

1. P. Mellor: *Int. Met. Rev.*, 1981, vol. 26 (1), pp. 1–20.
2. D. Wilson: *Int. Mater. Rev.*, 1990, vol. 35 (1), pp. 329–48.
3. F. Roters, P. Eisenlohr, L. Hantcherli, D.D. Tjahjanto, T.R. Bieler, and D. Raabe: *Acta Mater.*, 2010, vol. 58 (4), pp. 1152–1211.
4. W.F. Hosford and R.M. Caddell: *Metal Forming: Mechanics and Metallurgy*. Cambridge University Press, Cambridge, 2011.
5. W. Lankford, S. Snyder, and J. Bauscher: *Trans. ASM*, 1950, vol. 42, pp. 1197–32.
6. H. Bunge: *Krist. Tech.*, 1970, vol. 5 (1), pp. 145–75.
7. J.W. Bae, H.Y. Um, S.H. Lee, B.J. Min, S.Y. Kim, J.S. Chung, K.S. Park, M.H. Seo, and H.S. Kim: *Metall. Mater. Trans. A*, 2017, vol. 48A, pp. 1021–32.
8. A. Chamanfar and R. Mahmudi: *Metall. Mater. Trans. A*, 2006, vol. 37A, pp. 3477–87.
9. R. Schouwenaars, P.V. Houtte, E. Aernoudt, C. Standaert, and J. Dilewijn: *ISIJ int.*, 1994, vol. 34 (4), pp. 366–72.
10. P. Dawson, S. MacEwen, and P. Wu: *Int. Mater. Rev.*, 2003, vol. 48 (2), pp. 86–122.
11. G. Sachs: *Trans. Faraday Soc.*, 1928, vol. 24, pp. 84–92.
12. G. Taylor: *J. Inst. Met.*, 1938, vol. 62, pp. 307–24.
13. P. Van Houtte: *Texture Stress Microstruct.*, 1987, vol. 7 (1), pp. 29–72.
14. W.F.J. Hosford: *Mater. Sci. Eng. A*, 1998, vol. 257 (1), pp. 1–8.
15. P. Lequeu and J. Jonas: *Metall. Trans. A*, 1988, vol. 19A, pp. 105–20.
16. Y. Liu, S. Kang, and H. Ko: *Scr. Mater.*, 1997, vol. 37 (4), pp. 411–17.
17. P. Van Houtte: *Texture Stress Microstruct.*, 1988, vol. 8, pp. 313–50.
18. D. Daniel and J. Jonas: *Metall. Trans. A*, 1990, vol. 21 (1), pp. 331–43.
19. J. Savoie, J. Jones, S. MacEwen, and R. Perrin: *Textures Microstruct.*, 1995, vol. 23, p. 149.
20. S. Wronski and B. Bacroix: *Mater. Charact.*, 2016, vol. 118, pp. 235–43.
21. J.J. Park: *J. Mater. Process. Technol.*, 1999, vol. 87 (1), pp. 146–53.
22. J. Sidor, A. Miroux, R. Petrov, and L. Kestens: *Acta Mater.*, 2008, vol. 56 (11), pp. 2495–2507.
23. Y. An, R. Boterman, E. Atzema, M. Abspoel, and M. Scholting: *Metall. Mater. Trans. A*, 2016, vol. 47 (7), pp. 3435–46.
24. P. Wu, S. MacEwen, D. Lloyd, M. Jain, P. Tugcu, and K. Neale: *Int. J. Plast.*, 2005, vol. 21 (4), pp. 723–39.
25. N. Yoshinaga, N. Sugiura, S. Hiwatashi, K. Ushioda, and O. Kada: *ISIJ int.*, 2008, vol. 48 (5), pp. 667–70.
26. L. Delannay and M.R. Barnett: *Int. J. Plast.*, 2012, vol. 32, pp. 70–84.
27. D. Rees: *Appl. Math. Model.*, 1997, vol. 21 (9), pp. 579–90.
28. M. Huang and C.S. Man: *Int. J. Plast.*, 2013, vol. 41, pp. 97–123.
29. J. Ha, J. Lee, J.H. Kim, M.G. Lee, and F. Barlat: *Int. J. Plast.*, 2017, vol. 93, pp. 89–111.
30. J. Lee, J. Ha, H.J. Bong, D. Kim, and M.G.J. Lee: *Mater. Sci. Eng. A*, 2016, vol. 672, pp. 65–77.
31. Q. Xie, Y. Wang, A. Van Bael: Effect of the grain shape on the q-value evolution of steel sheets. In: *IOP Conference Series: Materials Science and Engineering*, vol. 82, p. 012096. IOP Publishing 2015.
32. J. Gawad, D. Banabic, A. Van Bael, D.S. Comsa, M. Gologanu, P. Eyckens, P. Van Houtte, and D. Roose: *Int. J. Plast.*, 2015, vol. 75, pp. 141–69.
33. J. Gawad, A. Van Bael, P. Eyckens, G. Samaey, P. Van Houtte, and D. Roose: *Comput. Mater. Sci.*, 2013, vol. 66, pp. 65–83.
34. L. Delannay, S. Kalidindi, and P.J. Van Houtte: *Mater. Sci. Eng. A*, 2002, vol. 336 (1), pp. 233–44.
35. M. Kraska, M. Doig, D. Tikhomirov, D. Raabe, and F. Roters: *Comput. Mater. Sci.*, 2009, vol. 46 (2), pp. 383–92.
36. B. Liu, D. Raabe, F. Roters, P. Eisenlohr, and R. Lebensohn: *Model. Simul. Mater. Sci. Eng.*, 2010, vol. 18 (8), p. 085005.
37. J. O'Brien, W. Hosford, and R. Logan: *Metall. Mater. Trans. A*, 1997, vol. 28 (10), pp. 2085–88.
38. L. Delannay, P. Van Houtte, A. Van Bael, and D. Vanderschueren: *Model. Simul. Mater. Sci. Eng.*, 2000, vol. 8 (4), p. 413.
39. B.L. Adams, A. Henrie, B. Henrie, M. Lyon, S. Kalidindi, H. Garmestani: *J. Mech. Phys. Solids* 2001, vol. 49(8), pp. 1639–63.
40. D.T. Fullwood, S.R. Niezgodna, B.L. Adams, and S.R. Kalidindi: *Prog. Mater. Sci.*, 2010, vol. 55 (6), pp. 477–562.
41. R. Liu, A. Kumar, Z. Chen, A. Agrawal, V. Sundararaghavan, and A. Choudhary: *Sci. Rep.*, 2015, vol. 5, p. 11551.
42. H.J. Bunge: *Texture Analysis in Materials Science: Mathematical Methods*. Elsevier, New York, 2013.
43. P. Van Houtte: *Texture Stress Microstruct.*, 1991, vol. 13, pp. 199–212.
44. P. Van Houtte: *Texture Stress Microstruct.*, 1983, vol. 6 (1), pp. 1–19.
45. P. Van Houtte: *The MTM-FHM Software System Version 2*, Users Manual, KU Leuven, 1995.
46. A. Khachatryan, S. Semenovskaya, and B. Vainstein: *Sov. Phys. Crystallogr.*, 1979, vol. 24, pp. 519–24.
47. Robbins, H., Monro, S. *Ann. Math. Stat.* 1951, pp. 400–407.
48. E. Anderson, Z. Bai, C. Bischof, S. Blackford, J. Demmel, J. Dongarra, J. Du Croz, A. Greenbaum, S. Hammarling, A. McKenney, and D. Sorensen: *LAPACK Users' Guide*, 3rd ed.,

Society for Industrial and Applied Mathematics, Philadelphia, PA, 1999.

49. J.G. Sevillano, P. Van Houtte, and E. Aernoudt: *Prog. Mater. Sci.*, 1980, vol. 25 (2-4), pp. 69-134.
50. M. Renouard and M. Wintenberger: *CR Acad. Sci. Paris B*, 1981, vol. 292, pp. 385-88.

51. P. Van Houtte: *Mater. Sci. Eng.*, 1982, vol. 55 (1), pp. 69-77.

52. P. Van Houtte, S. Li, M. Seefeldt, and L. Delannay: *Int. J. Plast.*, 2005, vol. 21 (3), pp. 589-624.
53. RA. Lebensohn and C. Tomé: *Acta Metall Mater.*, 1993, vol. 41 (9), pp. 2611-24.